Applied Materials Today 29 (2022) 101662

Contents lists available at ScienceDirect

Applied Materials Today

journal homepage: www.elsevier.com/locate/apmt

Reprogrammable flexible mechanical metamaterials

Xiaoyang Zheng [1,a,b], Koichiro Uto [1,c], Wei-Hsun Hu [a,d], Ta-Te Chen [a,b], Masanobu Naito [a,d], Ikumu Watanabe [a,b,*]

[a] Graduate School of Pure and Applied Sciences, University of Tsukuba, 1-1-1 Tennodai, Tsukuba 305–8573, Japan
[b] Research Center for Structural Materials, National Institute for Materials Science, 1-2-1 Sengen, Tsukuba 305-0047, Japan
[c] Research Center for Functional Materials, National Institute for Materials Science, 1-1 Namiki, Tsukuba 305-0044, Japan
[d] Research and Services Division of Materials Data and Integrated System (MaDIS), National Institute for Materials Science, 1-2-1 Sengen, Tsukuba 305-0047, Japan

ARTICLE INFO

Keywords:
Mechanical metamaterials
Shape-memory polymers
Soft robotics
Negative Poisson's ratios
Buckling
Imperfection

ABSTRACT

Mechanical metamaterials are artificial structures with structure-dependent properties. They often harness zero-energy deformation modes, e.g., a single shape change that limits their applications, resulting in the need for changeable mechanical responses. We address this limitation by using a flexible material, called light-responsive shape-memory polydimethylsiloxane (SM-PDMS), to introduce reprogrammability into flexible mechanical metamaterials. The SM-PDMS is a rubber-like functional material with shape-memory and photothermal effects. Specfically, we propose three different reprogrammable SM-PDMS metamaterials with different mechanical responses, namely, an auxetic SM-PDMS, a chiral SM-PDMS, and a buckling-induced SM-PDMS. Finally, a buckling-induced SM-PDMS was harnessed to make a soft actuator with a reprogrammable preferred locomotion direction. Despite focusing on reprogramming flexible metamaterials using the light-induced SM effect, our strategy can be easily extended to other structures and smart materials. More importantly, our strategy paves the way to change the mechanical responses for similar architectures. Furthermore, our designed flexible metamaterials have the potential for different applications, such as soft robots, actuation, adaptive safety, and sports equipment.

1. Introduction

Mechanical metamaterials are artificial structures with distinct properties attributed to their delicate architecture rather than their composition [1–3]. Manipulating the local cell geometries and their global spatial distributions and arrangements enables the design and creation of mechanical metamaterials with unprecedented properties and functions, such as an ultrahigh stiffness-to-weight ratio [4–7], negative Poisson's ratio [8–13], chirality [14], localized deformations [15–17], and multi-shape transformation [18–21]. Particularly, flexible mechanical metamaterials, which can recover their original shape after large deformations, exhibit great potential for application in soft robots [22–32], whose performance can be enhanced by the complex collective behavior of highly deformable flexible metamaterials. For example, auxetic metamaterials made of rubber-like materials can densely shrink in all three directions under a large uniaxial compressive load and recover to its original shape without fracture or failure [11]. Additionally, origami-inspired metamaterials can be designed to possess single-direction flexible motion while remaining stiff against other types of deformations [33].

Since being firstly proposed in 2014 in the electromagnetic regime [34], the concept of programmable metamaterial has been extended to acoustic, physics, thermal, and mechanics fields [35–40]. Programmability refers to the function that the properties of metamaterials can be designed and achieved via reconfigurable or digital coding approaches. Regarding mechanical metamaterials, the programmability can be harnessed to obtain a tunable stiffness [37], tailorable negative Poisson's ratio and arbitrary thermal expansion [39], and multiple deployable and reversible configurations [40], among other desirable properties. However, programmability is always achieved during the design process, and the material's mechanical responses are hardly changed after fabrication.

To have an impact on soft robots, flexible metamaterial reprogrammability is required. This allows changing the complex motion of

* Corresponding author at: Graduate School of Pure and Applied Sciences, University of Tsukuba, 1-1-1 Tennodai, Tsukuba 305–8573, Japan.
E-mail address: WATANABE.Ikumu@nims.go.jp (I. Watanabe).

[1] These authors contributed equally.

https://doi.org/10.1016/j.apmt.2022.101662
Received 27 June 2022; Received in revised form 23 September 2022; Accepted 18 October 2022
Available online 26 October 2022

soft robots directly by reprogramming the architecture itself, rather than fabricating a new one. Several strategies have been harnessed to achieve reprogrammability, such as combinatorial design [18,41,42], hybrid materials [43–45], association with additional physical fields [46–49], and using smart materials (e.g., shape-memory (SM) polymers and liquid crystalline elastomers) [30,31,50–52]. However, these previous studies have some limitations. For example, the deformation modes of hybrid mechanical metamaterials are highly dependent on the external environment (e.g., temperature and load rate). This implies that it is difficult to achieve a distinct deformation behavior under the same load condition [44,45]. To make the reprogrammability free from the external environment, a discrete assembly has been used to construct mechanical metamaterials [41]. Similar to Lego bricks, a finite set of parts can be spatially composed to achieve different properties, including rigidity, compliance, chirality, and auxetic behavior. To make it assembly-free with a distinct mechanical response under the same load, smart materials with changeable properties (e.g, SM polymers) have the potential to make continuous, monolithic structures with reprogrammability. However, mechanical metamaterials made of SM polymers hardly undergo large deformations due to the plasticity of SM polymers at room temperature (below the transition temperature) [30,31,53–55]. Therefore, it is desired to make reprogrammable mechanical metamaterials with SM polymers that can undergo large deformation and have stimulus-response properties.

To address these aforementioned limitations and challenges, we propose a novel strategy that combines imperfections with the SM effect to reprogram the deformation behavior of mechanical metamaterials. In this study, SM fillers and photothermal nanoparticles were combined with polydimethylsiloxane (PDMS), a rubber-like soft material, to impart light-responsiveness and SM capabilities (Fig. 1a). After receiving light stimulation, the proposed SM-PDMS becomes softer and reconfigurable above the melting point (T_m) because of the photothermal effect. The deformed shape remains after cooling to room temperature (below the crystallization temperature, T_c), and it recovers its original shape after further light stimulation. Guided by numerical analyses, we demonstrate the ability to harness the SM-PDMS to design three different flexible metamaterials with distinctive deformation modes, namely, an auxetic SM-PDMS, a chiral SM-PDMS, and a buckling-induced SM-PDMS, which exhibit reprogrammable expansion and shrinkage, twist, and rotation behaviors, respectively. Finally, for demonstration purpose, we show an application for manipulating the buckling-induced SM-PDMS to make an actuator capable of locomotion along a preferred direction after on-demand local stimulation. Furthermore, we expect the reprogrammability of SM-PDMS to be particularly advantageous in soft robotic applications requiring reversible, on-demand mechanical responses.

2. Experimental section

2.1. SM-PDMS preparation

The SM-PMDS was prepared by mixing the PDMS (10:1 mix ratio, Sylgard 184, The Dow Chemical Company, USA) with a SM filler (1,10-decanediol, TCI AMERICA, USA). Before mixing with the PDMS, the SM filler was milled into powder using a mortar and pestle mixing grinding bowl. Then, the photothermal effect was introduced by doping with 0.2 wt% TiN nanoparticles (Nisshin Engineering Inc., Japan). A Thinky PDMS Mixer (Thinky Mixer ARE-310, THINKY, USA) was used to efficiently mix, disperse, and deaerate the SM fillers, TiN nanoparticle, and PDMS mixture for 5 min. Thereafter, the well-mixed SM-PDMS was degassed in a polycarbonate desiccator under high-vacuum conditions for 30 min.

The SM-PMDS metamaterials and specimens used for the mechanical tests were fabricated using the molding method, as shown in Figs. A.1, A.2,A.3. These molds were designed using a computer-aided design software (3Ds max, Autodesk, USA), and their dimensions are shown in Figs. A.1b, A.2b, and A.3b, respectively. The designed molds were printed using a stereolithography three-dimensional (3D) printer (Form 3, Formlabs, USA) with a light-reactive thermoset resin (Clear Resin, Formlabs, USA). The molds were washed with isopropyl alcohol for 10 min, followed by curing at 60°C for 30 min. A hydrophobic layer was coated on the surface of the molds using 1H, 1H, 2H, 2H-perfluorodecyltrichlorosilane ($C_{10}H_4Cl_3F_{17}Si$, TCI AMERICA, USA) via chemical vapor deposition in a desiccator for 30 min to easily detach the SM-PDMS from

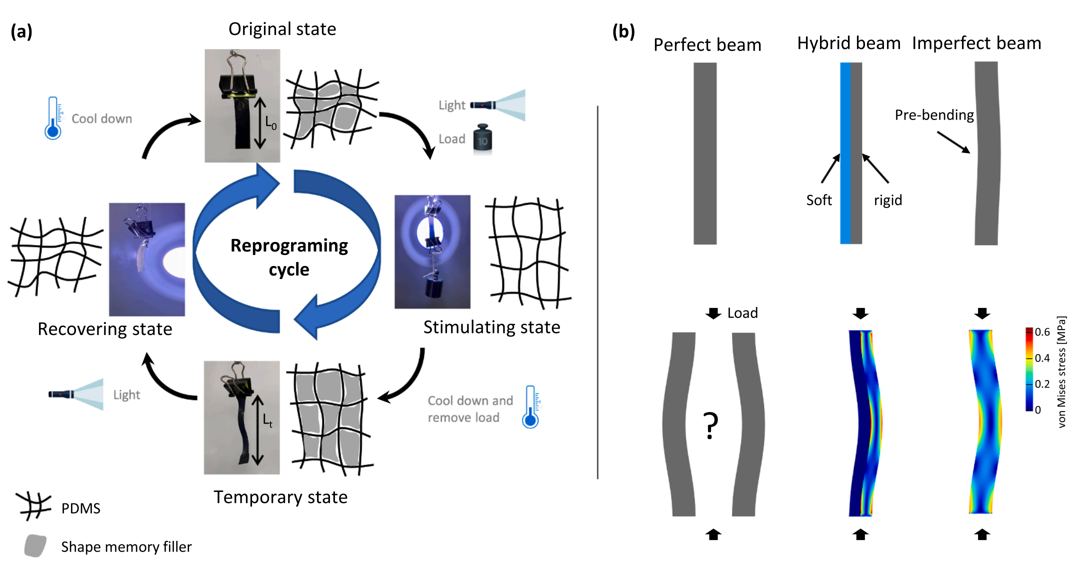

Fig. 1. Reprogramming the deformation behavior of a beam using the SM effect. (a) Photothermally-induced SM effect of a SM-PDMS. The SM-PDMS has an original length (L_0) and its SM filler component was solid (top insert). During photothermal stimulation and under a load, the SM filler was melted and the SM-PDMS was gradually stretched (right insert). After keeping the load until it cooled down, the SM filler solidified and the SM-PDMS kept a stretched temporary length (L_t) (bottom insert). The SM filler was melted after receiving local photothermal stimulation again, and the SM-PDMS gradually recovered to its original length (left insert). (b) Tuning deformation modes using a hybrid beam or applying pre-bending to form a geometric imperfection. The buckling direction of a SM-PDMS beam could be manipulated by either applying local stimulation to form a hybrid beam (corresponding to the stimulating state) or applying a pre-bending to form a geometric imperfection (corresponding to the temporary state).

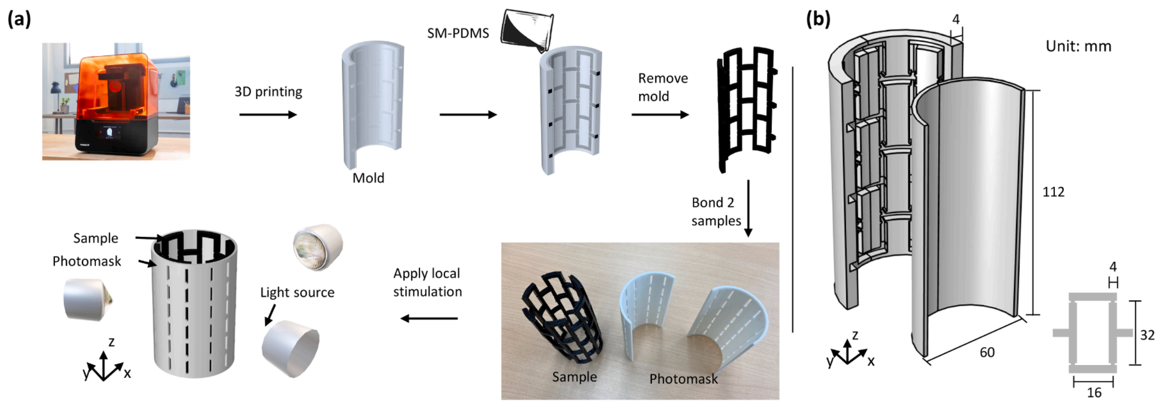

Fig. A1. Reprogramming a 3D auxetic metamaterial made of SM-PDMS. (a) Process of preparing a 3D auxetic metamaterial using 3D printing to make a mold, and the illustration of applying local light stimulation. (b) Mold design of a prepared 3D auxetic metamaterial.

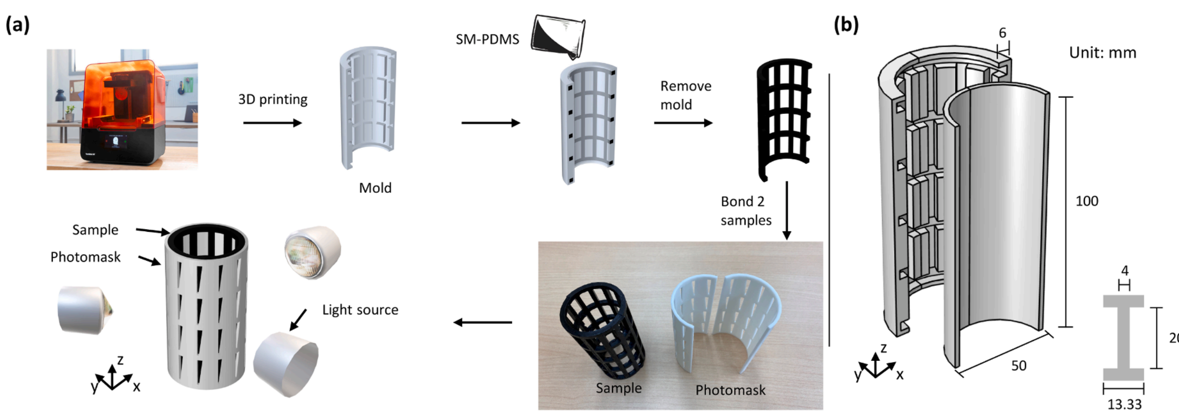

Fig. A2. Reprogramming a 3D chiral metamaterial made of SM-PDMS. (a) Process of preparing a 3D chiral metamaterial using 3D printing to make a mold, and the illustration of applying local light stimulation. (b) Mold design of a prepared 3D auxetic metamaterial.

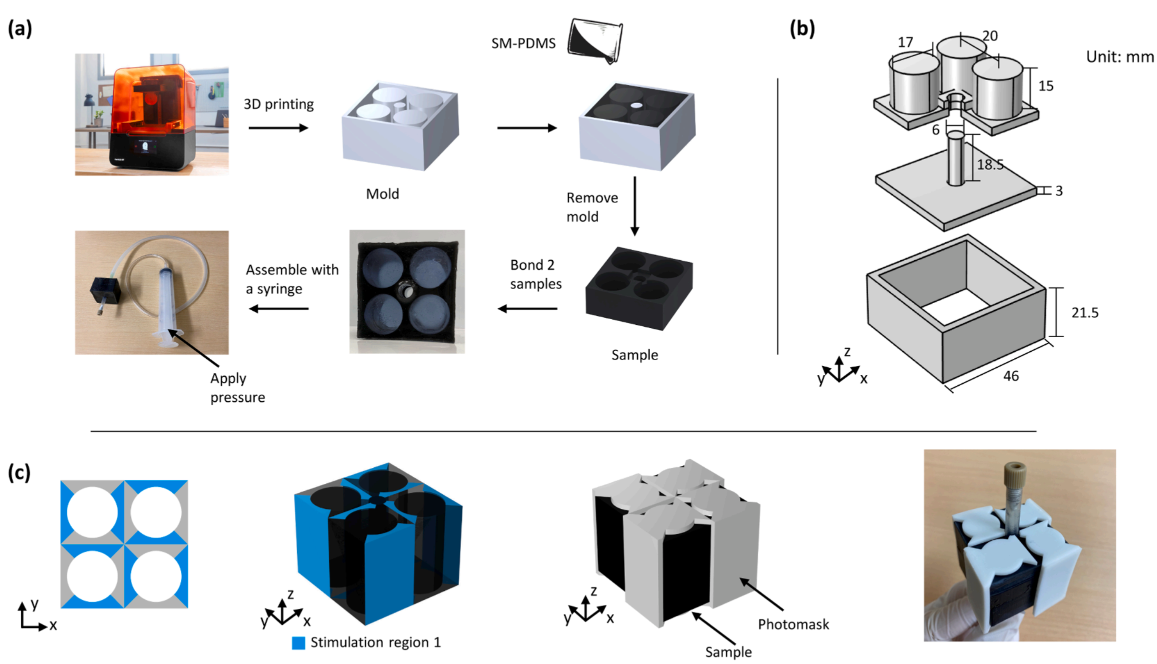

Fig. A3. Reprogramming a 2D buckling-induced metamaterial made of SM-PDMS. (a) Process of preparing a 2D buckling-induced metamaterial using 3D printing to make a mold. (b) Sample size of a mold for preparing the buckling-induced metamaterial. (c) Illustration of applying local light stimulation.

the molds. Subsequently, each mold was filled with uncured SM-PDMS, and was then baked for 24 h at 60°C. The specimens were finished by detaching them from the molds.

2.2. Mechanical properties investigation

Uniaxial tensile tests were performed using a motorized test stand (AG-Xplus-10kN, Shimadzu, Japan) at a constant displacement rate of 10 mm/min to evaluate the stress-strain curves and Young's moduli of the SM-PDMS specimens. ASTM D 412-06 (A) was used to assess the tensile properties of dog-bone (dumbbell)-type samples produced using 3D-printed dog-bone molds [56]. High-temperature tests were conducted in a thermostatic chamber (TCE-N300, Shimadzu, Japan).

In addition, the SM effect of SM-PDMS was evaluated using the fixity and recovery of the SM-PDMS dog-bone samples. First, an SM-PDMS dog-bone sample of the original length (L_0) was placed in a temperature-controlled motorized test stand. After heating to 100°C for 10 min, the sample was slowly extended to 40% strain (the length after stretching, L_s). Then, the sample was removed from the test stand after cooling to room temperature. The sample would slightly shrink and maintain a temporary length (L_t) owing to internal stress after releasing the load. Subsequently, the samples were placed in an oven at 100°C for 10 min. The samples almost recovered their initial shape and maintained a permanent length (L_p). The process was repeated five times for each sample to obtain the average fixity and recovery values. The strain of the SM-PDMS samples at each step was calculated as $\varepsilon_i = \ln(L_i / L_0)$, for $i = s, t, p$. The fixity (R_f) and recovery (R_r) are then given by $R_f = \varepsilon_t / \varepsilon_s$ and $R_r = (\varepsilon_s - \varepsilon_p/(\varepsilon_s - \varepsilon_0)$, respectively.

The fatigue test of the SM-PDMS samples was performed via dynamic mechanical analysis (DMA, DMA-242E, Netzsch, Germany) according to ASTM E1640–18 [57]. The DMA tests were conducted on cylindrical specimens with a radius of 3 mm and height of 5 mm, a heating rate of 1°C/min, and frequency of 5 Hz. The DMA chamber was heated and cooled to 100°C for 20 min and then further cooled to 50°C for 20 min. This process was repeated nine times. During each hold time, three load-unload cycles with a maximum stress of 10 kPa were applied to the samples.

The melting point (T_m) of the SM-PDMS samples with different weight ratios of the SM filler was monitored via differential scanning calorimetry (DSC-60, Shimadzu, Japan). Approximately 10 mg of each SM-PDMS sample was placed inside an aluminum pan with a pierced lid. The sample was heated to 150°C and held for 10 min at a scanning rate of 10°C/min under a nitrogen flow of 100 mL/min.

Compression tests were conducted using a motorized test stand (JSV-H1000-10N, JISC, Japan) at a constant displacement rate of 10 mm/min. Before the tests, local light stimulation was applied to each specimen using a high-brightness lighting box (LLBGR-A-15 $\times$ 20 $\sim$ 25 $\times$ 15, AITEC SYSTEM, Japan) with an irradiance of 800 W $/(\mathrm{m}^2{\cdot}\mathrm{sr})$ for 30 s. During light irradiation, the surface of each specimen was covered with a delicately designed photomask printed using a non-transparent resin (White Resin, Formlabs, USA). During the compression tests, the deformation processes of the specimens were observed using a high-speed camera.

2.3. Finite element method simulations

Finite element method (FEM) simulations were conducted to investigate the mechanical response of SM-PDMS metamaterials using a FEM simulation platform (COMSOL Multiphysics Ver. 5.6, COMSOL, Sweden). The constitutive material model of SM-PDMS was fitted to the tensile tests using a six-parameter hyperelastic material model (i.e., the Ogden material model) [58–61]. For the SM-PDMS with 30 wt% SM filler, the material parameters were set as $[\mu_1, \mu_2, \mu_3] = [-0.79, -3.96, 3.37]$ MPa and $[\alpha_1, \alpha_2, \alpha_3] = [1.83, -3.25, -2.8]$ at room temperature (i.e., non-stimulated region), and $[\mu_1, \mu_2, \mu_3] = [0.01, -5.12, 14.43]$ MPa and $[\alpha_1, \alpha_2, \alpha_3] = [4.00, -0.36, 0.11]$ above T_m (stimulated region), respectively. The models were meshed using approximately $1 \times 10^5 \sim 3 \times 10^5$ second-order triangular solid elements for the two-dimensional (2D) geometries and second-order tetrahedral solid elements for the 3D geometries. Specifically, simulations of the 2D auxetic SM-PDMS and chiral SM-PDMS were performed under periodic boundary conditions as the 2D auxetic SM-PDMS and chiral SM-PDMS metamaterials were periodic. The method applied periodic boundary conditions to pairs of faces of the unit cell based on a representative volume element technique [62,63].

A multiphysics coupling (heat transfer with radiation in absorbing scattering media) simulation was performed using COMSOL to simulate the photothermal response of an SM-PDMS beam receiving local light. In particular, it allowed heating to be computed because of radiation absorption. A 2D model (rectangle) was used with a thermal conductivity of 0.16 W/m/K, heat capacity of 2005 J/kg/K, absorption coefficient of 293 cm^{-1}, and scattering coefficient of 1.4 m^{-1} [64,65]. The top right surface of the rectangle was radiated with an incident intensity of 800 $\mathrm{W}/(\mathrm{m}^2{\cdot}\mathrm{sr})$. The P1 approximation discretization method was applied to the simulation because the model was based on linear anisotropic scattering [66].

3. Materials design strategy

The basic idea of this study was to harness either material or geometric imperfections to reprogram the deformation modes of flexible metamaterials (see Fig. 1b). Considering a beam under a compressive uniaxial load as an example, it was difficult to predict the bending direction for a perfect beam. However, if the beam was hybrid and composed of laterally attached beams (made of two materials with different stiffnesses), it would predictably buckle to the stiffer side (when loaded slowly in compression). Another way to predict the bending direction was by introducing geometric imperfections. The beam would bend on its curved side if it has an initial curvature.

We found that these requirements were satisfied using SM-PDMS as a constituent material, as shown in Fig. 1. SM-PDMS is a rubber-like material that maintains its permanent shape at room temperature. It becomes softer and reconfigurable after heating over its T_m by receiving light due to the photothermal effect and retains the temporarily deformed shape after cooling. This process is known as the programming process. It can return to its permanent (original) shape from the temporarily deformed shape by reheating, paving the way to reprogram it. SM-PDMS was prepared by physically mixing PDMS with a SM filler (i.e., 1,10-decanediol), followed by doping with plasmonic titanium nitride (TiN) nanoparticles to enable precise photothermal stimulation. PDMS is elastic, transparent, biocompatible, and gas-permeable, and can achieve more functionalities via surface and bulk modifications. For example, its stiffness can be tuned by changing the mixing ratio and it can become electrically and thermally conductive by embedding free molecules, nanoparticles, or by altering the composition of the base elastomer before polymerization. These characteristics make it a suitable candidate for soft robotics and actuators [22–25,29]. TiN nanoparticles, a broadband plasmonic light absorber, are responsive to sunlight and thus can locally heat their surrounding [67]. SM-PDMS was physically entrapped with solid crystalline small molecules of SM filler that induced a reversible phase transition in the permanent network (crosslinked PDMS). The permanent network was a hyperelastic network that maintained a permanent shape and recovery after a large deformation. The entrapped SM filler, which dominates the SM effect, can fix a temporary shape by counterbalancing the load stored in the permanent network.

The stiffness needs to be investigated first to harness the SM-PDMS to reprogram flexible metamaterials. We demonstrated the ability to tune the stiffness of SM-PDMS over a wide range (Fig. 2a and b). Fig. 2a shows the stress-strain curves of dog-bone test specimens with different SM

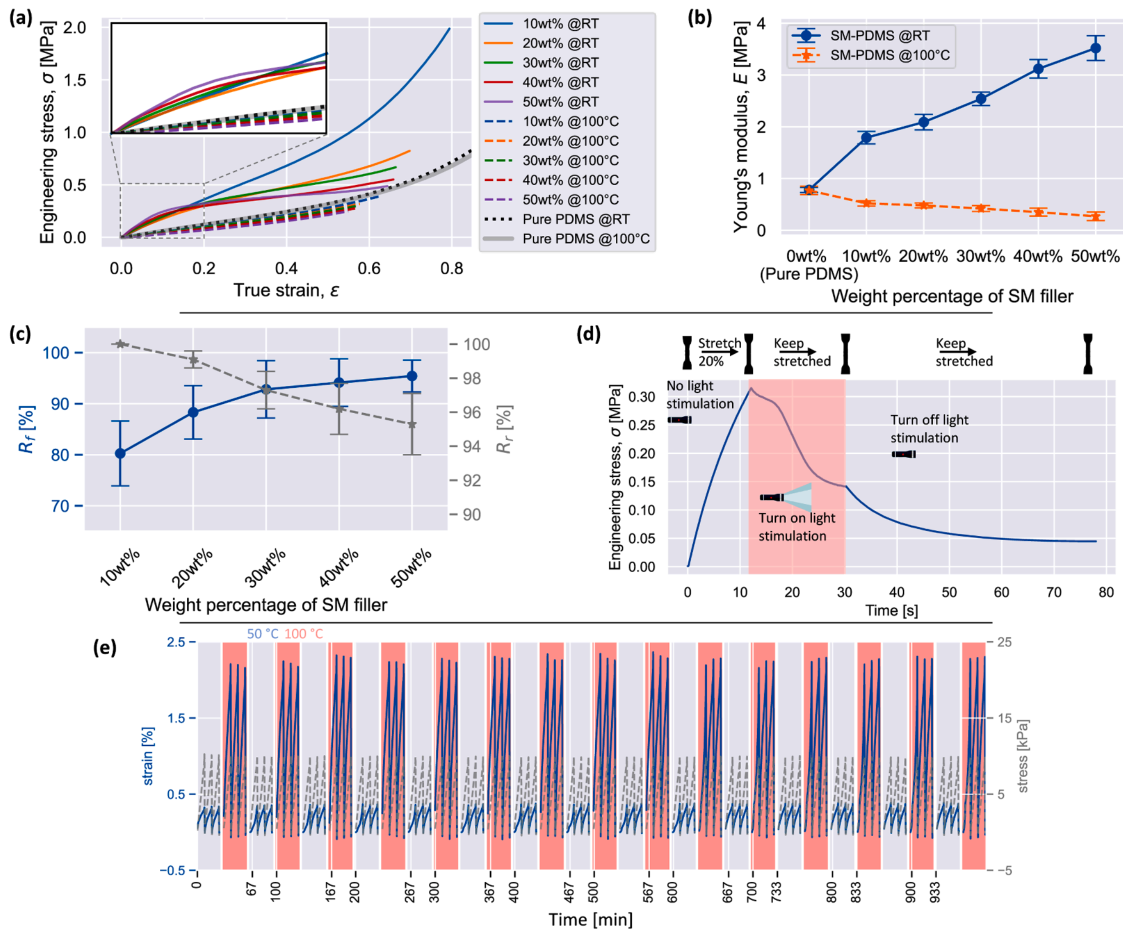

Fig. 2. Material properties of the constituent material (photothermally-induced SM-PDMS) for mechanical metamaterials. (a) Stress-strain curves of SM-PDMS ($T_m \approx$ 76°C) at 50 °C and 100°C. (b) Effective Young's modulus versus the weight percentage of SM filler. (c) Shape fixity (R_f) and recovery (R_r) versus the weight percentage of SM filler. (d) Light-response test of a dumbbell-type SM-PDMS sample with 30 wt% SM filler content. The sample was stretched 20% before given light stimulation. The light stimulation was turned off after the stress became stable. The stress did not reach to the original zero value due to the residual stress in PDMS. (e) Fatigue test of an SM-PDMS sample with 30 wt% SM filler content..

filler weight percentages. They were fitted using the Ogden hyperelastic material model to calculate the Young's modulus at a small strain ($E = \frac{3}{2}\sum_{i=1}^{3}\mu_i\alpha_i$), as shown in Fig. A4. Importantly, the SM-PDMS exhibited an elastic behavior in the low-strain region even in the hard state below the melting point. This was clearly different from the general SM polymers that exhibited plastic properties under similar conditions. As shown in Fig. 2b, the Young's modulus at room temperature increased from 0.78 to 3.52 MPa as the SM filler increased from 0 to 50 wt%. The Young's modulus at 100°C (above T_m) decreased from 0.78 to 0.27 MPa. A similar tendency in terms of the shear modulus is also shown in Fig. A5. This indicated that increasing the weight percentage of the SM filler can increase the stiffness difference between the SM-PDMS before and after local stimulation. A stiffness difference of six times could be achieved for an SM-PDMS with 30 wt% SM filler. Note that the T_m and T_c of the SM-PDMS were barely affected by the weight percentage of the SM filler and were maintained at approximately 76°C and 64°C, respectively, based

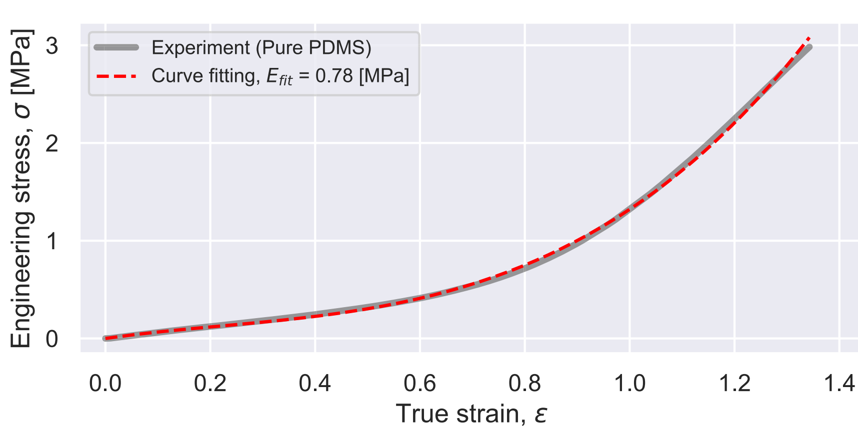

Fig. A4. Curve fitting of a typical stress-strain curve for a dogbone specimen of an SM-PDMS using the Ogden hyperelastic material model.

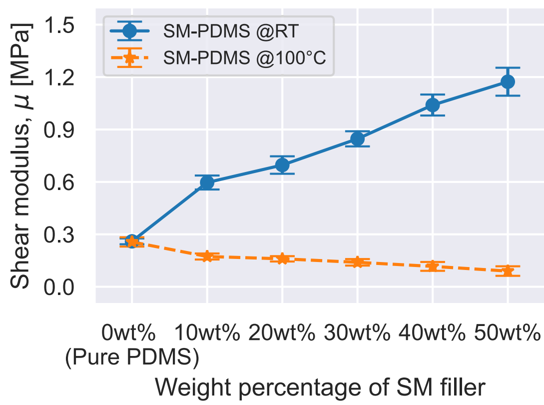

Fig. A5. SM-PDMS Shear modulus with different SM filler.

on the differential scanning calorimetry (DSC) thermal analysis (see Fig. A6). The DSC thermal analysis was carried out at $-50 \sim 150°C$, and there was no damage found on the SM-PDMS. For the sake of application, room temperature is the suitable ambient surrounding for the proposed SM-PDMS metamaterials.

Geometric imperfections are highly associated with two SM factors: shape fixity (R_f) and recovery (R_r). R_f is the ability of SM-PDMS to fix its temporary shape during the programming process, whereas R_r is the ability of SM-PDMS to recover its permanent shape during the reprogramming process. R_f was dominated by the reversible phase (SM filler), whereas R_r was dominated by the permanent network (PDMS). Fig. 2c shows the effect of filler weight percentage on R_f and R_r. The results showed that with an increase in the filler weight percentage, R_f increased from approximately 80% to 95%, whereas R_r remained above 95%. The SM-PDMS sample with 30 wt% SM filler had an R_f of 93% and R_r of 97%. Geometric imperfections could be achieved by applying pre-bending to a locally stimulated beam, as shown in Fig. 1b. That is, a compressive load was applied on a beam after local stimulation, and the beam would keep a bent status if the load was kept until cooling to room temperature. The magnitude could be controlled by applying different compressive strains on the beam.

Considering the mechanical properties and SM effect, the SM-PDMS with 30 wt% SM filler had a suitable reprogrammable performance (i.e., six-time stiffness difference before and after local stimulation; $T_m = 76°C$; $T_c = 67°$; $R_f = 93\%$; and $R_r = 97\%$) and was used for fabricating mechanical metamaterials. The recovery of the material after deformation is called a deforming cycle, and changing the deformation mode is called a reprogramming cycle. To investigate the fatigue resistance of SM-PDMS, we conducted two 1000-cycle load-unload tests on a dumbbell-type SM-PDMS sample (with 30 wt% SM filler) at room temperature and 100°C, respectively. For each deforming cycle, the sample was stretched to 20% and then released to its original length. The stress was measured and the results are shown in Fig. A7. The results show that the stress repeated well even after 1000 load-unload cycles for the test at room temperature; however, for the test at 100°C, the peak stress

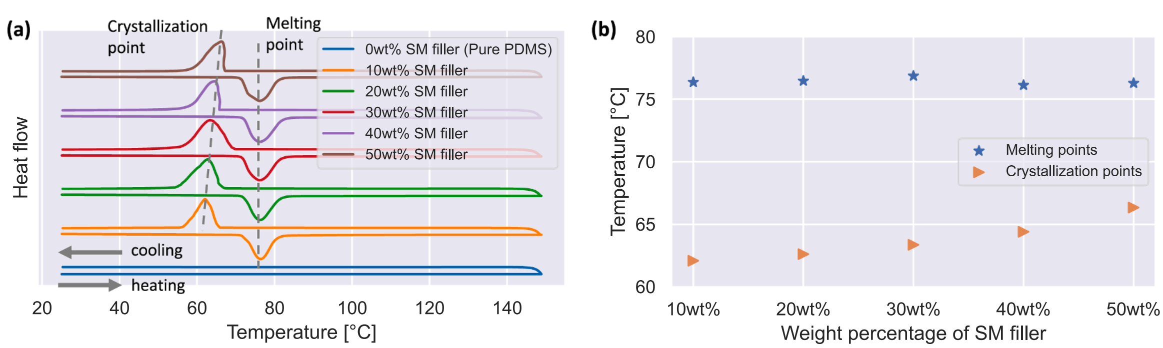

Fig. A6. (a) DSC curves of SM-PDMS samples with different SM filler weight percentage. (b) Melting and crystallization temperatures versus SM filler weight percentages.

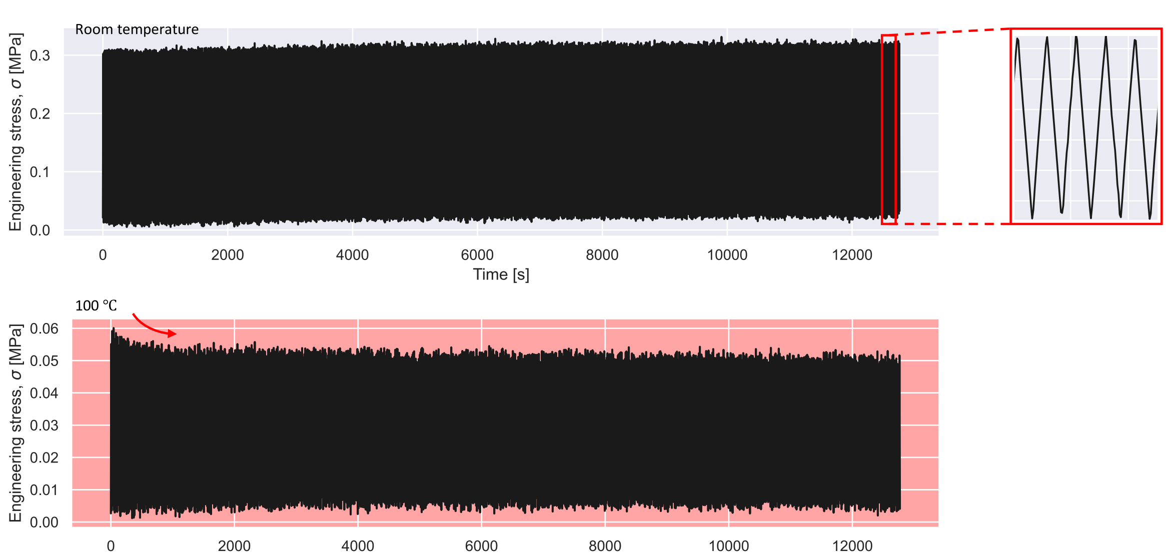

Fig. A7. Load–unload tensile tests of a dumbbell-type SM-PDMS sample with 30 wt% SM filler at (a) room temperature and (b) 100 °C.

gradually decreased initially, which can be attributed to SM filler loss. Because the SM filler was physically mixed with the PDMS rather than via chemical bonding, some of the SM filler on the surface would flow out after melting while being driven by the repeatedly pressing, softening the SM-PDMS. However, as the proposed SM-PMDS metamaterials are actuated at room temperature and the high temperature is just used to change their deformation modes, they can keep anticipative mechanical responses for their practical applications. Furthermore, we also investigated the reprogramming cycles using via DMA. The change in strain was measured to evaluate the repeatability by maintaining a certain stress (10 kPa) and varying the temperature (50–100°C). To demonstrate this, 15 load-unload cycles were applied to an SM-PDMS sample with 30 wt% SM filler at 50°C (below T_c). Then, the temperature was gradually increased to 100°C (above T_m), followed by the application of another load-unload cycle on the sample. After cooling to 50°C, load–unload cycles were performed again on the sample. The SM-PDMS sample could sustain 15 heating–cooling cycles without fracture (see Fig. 2e), showing acceptable repeatability.

To precisely measure the response time of the reprogramming process, we conducted a photothermal response test on a pre-stretched dumbbell-type SM-PDMS sample (Fig. 2d). The sample was pre-stretched at 20% tensile strain, and then light irradiation was applied on the sample's surface. The stress was monitored, which sharply decreased for 15 s and gradually converged under light irradiation. This is because the sample became soft when heated above its melting temperature due to the photothermal effect. The light irradiation was kept for 20 s and was turned off after the stress became stable. Afterward, the stress gently decreased because the SM-PDMS was almost fixed to the deformed shape after cooling. It is worth noting that a small residual stress remained after fixing the SM-PDMS, which further demonstrates that the SM-PDMS cannot perfectly keep its deformed shape (i.e., the fixity is less than 100%, as shown in Fig. 2c). A demonstration of how to harness local light stimulation to create a hybrid beam with material imperfections is shown in Fig. 1b, where a beam buckles to the right after left-side local stimulation. The preferred buckling is due to the softening of the left-side part owing to the photothermal effect by doping plasmonic nanoparticles. Fig. A8 demonstrates the temperature and phase changes of the hybrid beam under light radiation, which makes local light stimulation possible. In our experiments, light irradiation was carried out for approximately 30 s to ensure the locally simulated parts were sufficiently heated, and the cooling process was carried out for approximately 30 s. Consequently, it takes approximately 1 min for one reprogramming process.

4. Reprogrammable mechanical metamaterials

Given that the SM-PDMS had acceptable reprogrammability, we showed how to harness this to design and make three different flexible metamaterials with the desired deformation behavior. This was done in combination with bending, twisting, and buckling of basic elements of metamaterials that responded to a load. The deformation mode of each flexible metamaterial can be converted under ambient conditions using delicately controlled local stimulation by creating SM-PDMS metamaterials with spatially controlled arrangements of their basic elements.

4.1. Auxetic metamaterial

First, we propose an auxetic SM-PDMS whose deformation mode could be reprogrammed to switch from contraction to expansion under uniaxial compressive loading. Auxetic metamaterials are mechanical metamaterials with a negative Poisson's ratio [9–12]. As the expansion or contraction can be quantitatively measured using the Poisson's ratio, the auxetic SM-PDMS shows either a positive or negative Poisson's ratio on demand. The basic element of an auxetic SM-PDMS is a beam that can bend to either the left or right, depending on the local stimulation region, as shown in Fig. 3a. The bending direction of the beam was theoretically analyzed based on Euler's buckling theory for beams on elastic foundations (see Appendix A). According to this theory, a hybrid beam buckles to the stiffer side under a longitudinal compressive load. A hybrid SM-PDMS beam can be achieved by applying local light stimulation to the left or right region of the beam as the SM-PDMS becomes partially soft after local stimulation. The slenderness ratio of the beam (height/width, h/w) was set below 8 (Fig. A9) to prevent the beam from higher order buckling modes.

The 2D auxetic SM-PDMS consists of beams assembled in a stretcher bond pattern, as shown in Fig. 3b. The brick pattern is designed to achieve a reprogrammable shrinkage and expansion behavior. Unlike re-entrant auxetic metamaterials consisting of concave polygons, the 2D auxetic SM-PDMS is composed of rectangles. The vertical ligaments make it possible to bend right or left depending on local imperfections. Two factors were considered to realize the features of auxetic SM-PDMS: (i) Mechanical properties (Young's modulus and Poisson's ratio) were tunable via three independent geometric parameters (i.e., beam width w, beam height h, and distance between adjacent beams d) before fabrication; and (ii) Deformation modes (contraction and expansion) were reprogrammable using local stimulation after fabrication. We used the FEM calculations to analyze the effects of the three independent geometrical parameters on the Young's modulus and Poisson's ratio of

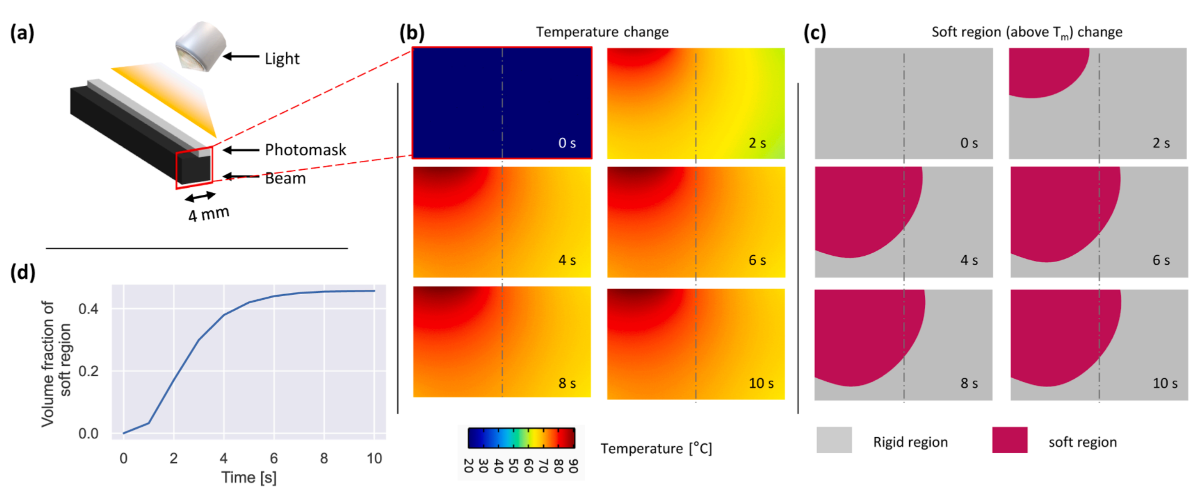

Fig. A8. Simulation of the photothermal response of a SM-PDMS beam receiving local light. (a) Illustration of applying local light stimulation. (b) Progressive temperature change sequence of a beam receiving local stimulation. (c) Progressive phase change sequence of the beam receiving local stimulation. (d) Phase change of the beam receiving local stimulation. The beam becomes almost half rigid and half soft after receiving local light stimulation.

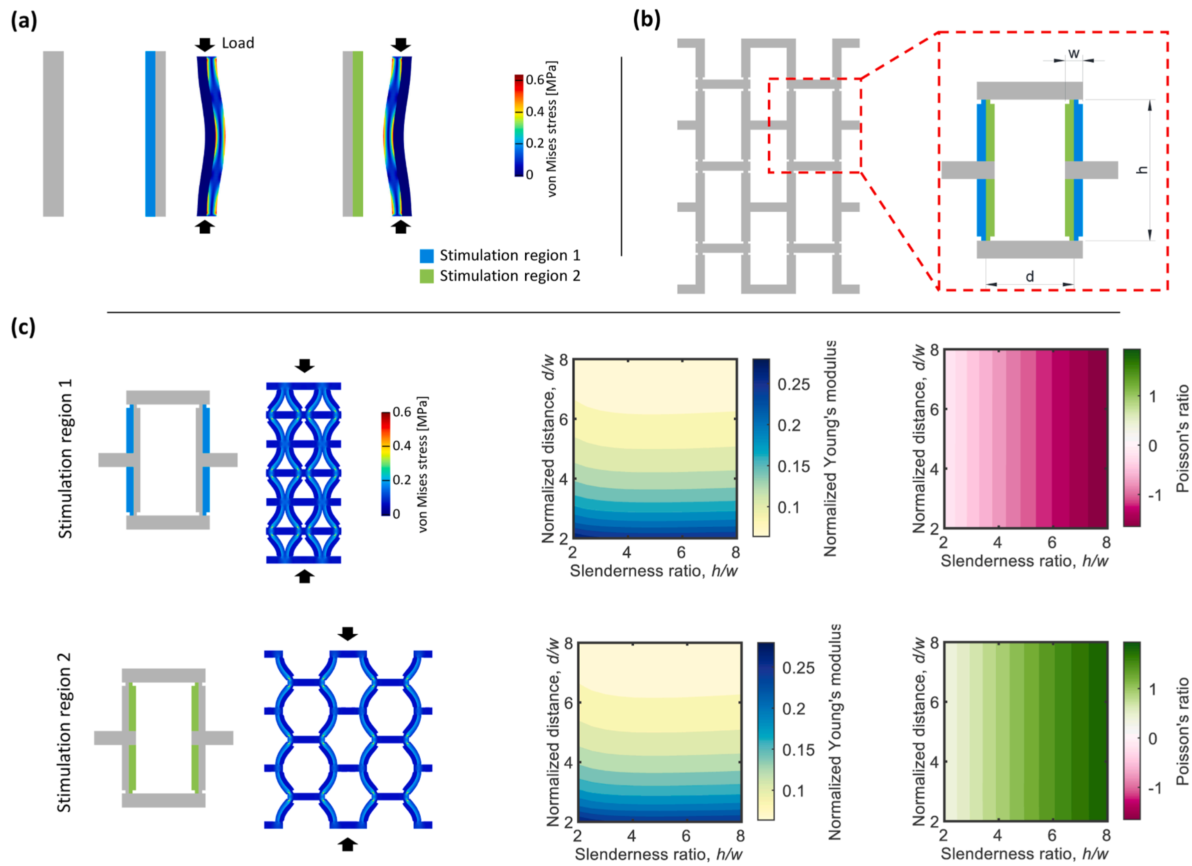

Fig. 3. 2D Reprogrammable auxetic metamaterial. (a) Basic beam element. The buckling direction of the beam can be controlled using different local photothermal stimulation. (b) 2D auxetic metamaterial consisting of multiple beams with tunable geometric parameters. (c) Tunable Young's modulus and Poisson's ratio of the 2D auxetic metamaterial based on different geometric parameters and controllable deformation modes (shrinkage or expansion) based on different stimulation regions.

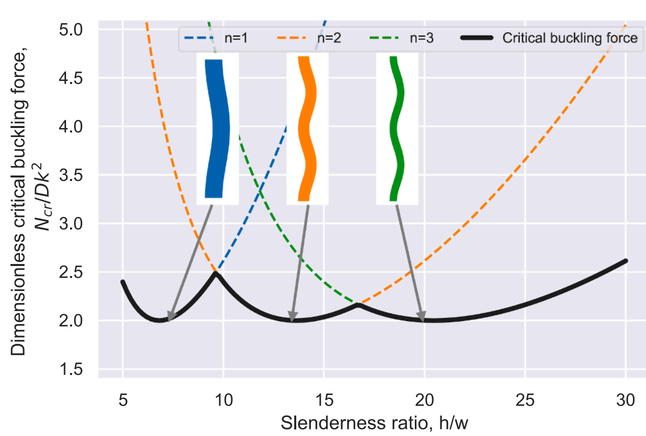

Fig. A9. Buckling analysis of a hybrid beam. The beam tends to buckle with higher-order model if the slenderness ratio is over 12.

the 2D auxetic SM-PDMS, as shown in Fig. 3c. The 2D auxetic SM-PDMS was also compared with some typical auxetic metamaterials in terms of Young's modulus and Poisson's ratio, as shown in Fig. A.10a. It shows that the Poisson's ratios of our proposed auxetic SM-PDMS cover a square area, exhibiting both positive and negative values. For the sake of comparison with the experimental results, the beam width was set as a constant w = 4 mm, whereas the beam height (defined as the slenderness ratio, h/w) and the distance between adjacent beams (defined as the normalized distance, d/w) were changed based on parametric sweeping calculations. Based on the FEM simulation results, the Young's modulus of the 2D auxetic SM-PDMS was highly dependent on d/w. The Young's modulus became smaller as d/w increased. In contrast, the Poisson's ratio was less sensitive to d/w but was significantly affected by h/w; it approached zero as h/w decreased. It is worth noting that changing the local stimulation region did not affect the Young's modulus; however, it converted the Poisson's ratio from negative to positive. This further demonstrated that local stimulation could be manipulated to reprogram the deformation modes from contraction to expansion, and vice versa, without stiffness loss.

Furthermore, we conducted an application case for making an auxetic SM-PDMS 3D hollow cylinder out of the 2D auxetic SM-PDMS, which was folded using the 2D auxetic SM-PDMS with 12×3 unit cells. The 3D cylindrical auxetic SM-PDMS exhibited imperfection-dependent deformation modes, shrinking or expanding laterally under a compressive load, depending on different local stimulation regions. Fig. 4a shows a typical reprogrammable cycle. However, if local stimulation was applied to the region outside a unit cell (blue region), the 3D cylindrical auxetic SM-PDMS shrunk laterally under a compressive load. After receiving global light, it recovered to the original shape. Then, it expanded laterally if local stimulation was applied to the region inside a unit cell (green region). A specimen made via 3D printing and templating is shown in Fig. A.1a and b, where a 3D auxetic SM-PDMS was made by pouring uncured SM-PDMS into 3D-printed molds and bonding the separated samples together. Local stimulation was achieved using a cylindrical photomask with specific pore arrangements, as shown in Fig. A.1a. Uniaxial compressive tests were performed on the specimens after receiving different local stimulation. Before each compressive test, the specimen recovered its original shape under global light stimulation.

Fig. 4 b shows the sequence of progressively deformed shapes of the 3D auxetic SM-PDMS specimen under five different compressive strain

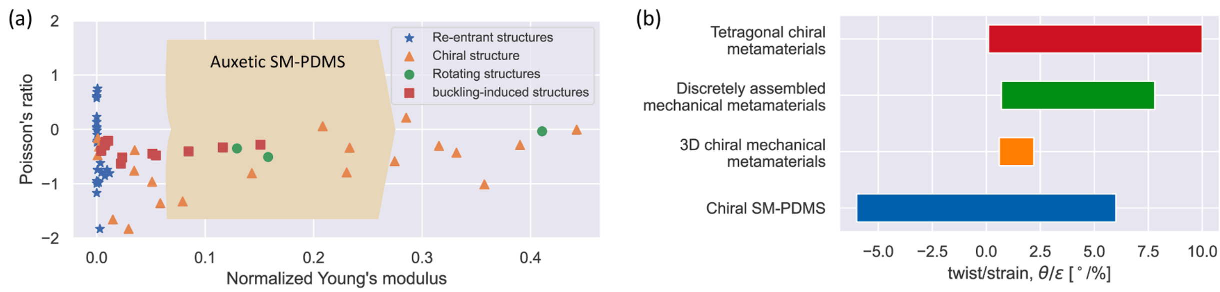

Fig. A10. Comparison between the proposed auxetic and chiral SM-PDMSs and some typical mechanical metamaterials. (a) Comparison between the auxetic SM-PDMS and re-entrant, chiral, and rotating structures [10,11,78–84]. The auxetic SM-PDMS has a Young's modulus and Poisson's ratio space covering a wide, near square region. (b) Comparison between the chiral SM-PDMS and tetragonal chiral metamaterials, discretely assembled mechanical metamaterials [14,41,85], and 3D chiral mechanical metamaterials. The chiral SM-PDMS has a wider twist/strain region covering from positive to negative. The twist/strain is calculated by the twist angle divided by the applied strain.

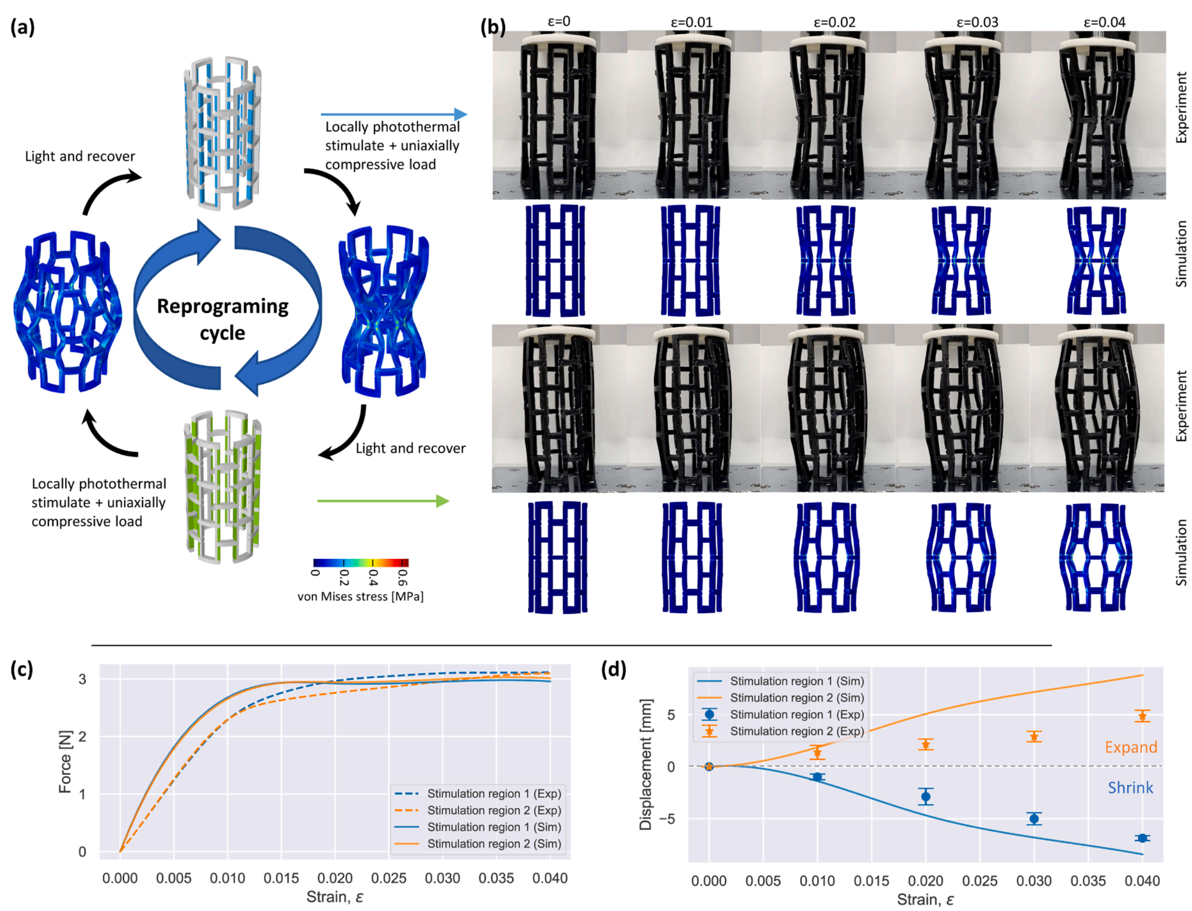

Fig. 4. 3D Reprogrammable auxetic metamaterial. (a) Typical reprogrammable cycle of a 3D auxetic metamaterial that is capable of either shrinking or expanding based on different local stimulation. (b) Sequence of progressively deformed configurations of the 3D auxetic metamaterial receiving different local stimulation. (c) Stress-strain curves of the 3D auxetic metamaterial with different local stimulation under a compressive load. (d) Lateral displacement of the 3D auxetic metamaterial with different local stimulation under a compressive load.

levels using different local stimulation (see the animation in Video S1). The experimental results relatively correlated with the FEM simulation results (i.e., the 3D cylindrical auxetic SM-PDMS shrunk or expanded after different local stimulation). However, it was noted that global buckling was triggered in the testing samples, which is mainly attributed to the cylinder's slenderness ratio, the wall thickness, and manufacturing error. To manufacture the SM-PDMS metamaterials, the molding method was used, where molds were 3D printed and filled with uncured SM-PDMS. These SM-PDMS metamaterials were obtained after detaching them from the molds, in which some parts would be destroyed, resulting in local nonlinear effects during deformation. When applying actuation, the overall performance and desirable functions may be degraded by these imperfections because such small dimensional errors can propagate to the entire mechanical metamaterials. To prevent such dimensional errors, it is recommended to make the mechanical metamaterials via direct 3D printing without support structures. Here, these small dimensional errors may result in global buckling. Thus, we tried to prevent global buckling by using a relatively low slenderness ratio (approximately 2) and a thick wall thickness (6 mm). Further, another efficient way to prevent this was to apply pre-bending on the hollow cylinders that had been discussed previously [68]. In addition, the imperfection-dependent deformation modes were validated by quantitatively evaluating the stress-strain curves and Poisson's ratios under different compression strains. For the same 3D SM-PDMS specimen under different local stimulation, the two stress-strain curves almost overlapped with each other and were independent of local stimulation, whereas the lateral displacements exhibited the opposite changing tendencies (Fig. 4c and d). The difference between simulated and experimental results is attributed to laboratory errors (from devices), human force, and incomplete contact with sample holders, whereas these errors were not considered in the simulations. More importantly, the difference between the simulated and experimental displacement largely resulted from hysteresis effects due to the incomplete contact between the sample's upper and bottom surfaces with the compression plates. These results further demonstrate that the 3D cylindrical auxetic SM-PDMS has reprogrammable contraction and expansion deformation modes using local stimulation without sacrificing stiffness.

4.2. Chiral metamaterial

Next, we propose a chiral SM-PDMS whose deformation modes could be reprogrammed from twisting clockwise to counterclockwise under an uniaxial compressive load. Chiral mechanical metamaterials, which exhibit handedness out of non-centrosymmetry, produce out-of-plane deformation modes (e.g., twisting) as a result of in-plane loads [14,69,70]. In contrast to common chiral mechanical metamaterials, whose deformation mechanism is attributed to node rotation and ligament bending, the chiral SM-PDMS has a unique deformation mechanism that is attributed to ligament leaning. Moreover, the basic element of a chiral SM-PDMS is a beam that could lean either to the left or right, depending on the local stimulation region, as shown in Fig. 5a. The stimulation and non-stimulation regions are rotationally symmetric, and the leaning direction can be tuned by the tilt angle α that divides the two regions.

Fig. 5b shows the 2D chiral SM-PDMS consisting of beams assembled in a stack-bond pattern. The pattern is designed to show the possibility to achieve compression-twist deformation without geometrical chirality. Two factors were considered to determine the chiral SM-PDMS features: (i) Mechanical properties (Young's modulus and twist angle) were tunable via three independent geometry parameters (i.e., w, h, and d) before fabrication; and (ii) Deformation modes (lean to the left or right) were reprogrammable using local stimulation after fabrication. FEM analyses were used to investigate the effects of the three independent geometry parameters on the Young's modulus and twist angle of the 2D auxetic SM-PDMS, as shown in Fig. 5c. The chiral SM-PDMS was also compared with some chiral mechanical metamaterials in terms of twist angle, as shown in Fig. A.10b. It shows that the twist angles of our proposed chiral SM-PDMS cover both positive and negative ranges. The beam width was set as a constant $w = 4$ mm, whereas the beam height (defined as h/w) and the tilt angle α were changed. The normalized Young's modulus of the 2D auxetic SM-PDMS was determined by both h/w and α. The Young's modulus increased as h/w decreased or α approached 90°. Conversely, the twist angle was highly sensitive to α and had a maximum absolute value when α approached 90°. Therefore, α should be set appropriately to maximize the absolute value of the twist angle. With an increase in h/w from 2 to 8, α could

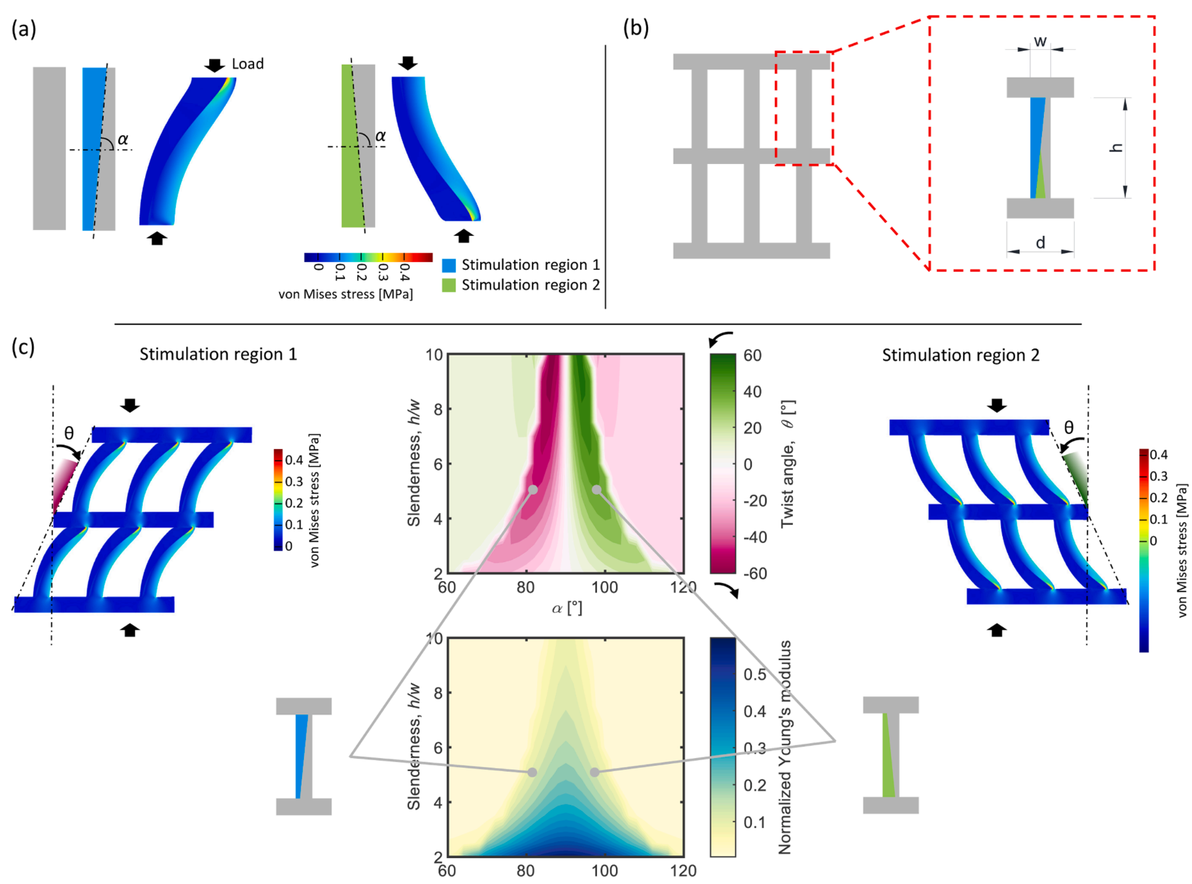

Fig. 5. 2D Reprogrammable chiral metamaterial. (a) Basic beam element. The leaning direction of the beam can be controlled using different local photothermal stimulation. (b) 2D auxetic metamaterial consisting of multiple beams with tunable geometric parameters. (c) Tunable Young's modulus and twist angle of the 2D auxetic metamaterial based on different geometric parameters, and controllable deformation modes (leaning to the left or right) based on different stimulation regions. The twist angles were calculated under a 0.1 compressive strain.

either increase from 72° to 86° to reach the maximum twist angle (leaning to the right) or decrease from 108° to 94° to reach the minimum twist angle (leaning to the left). This further demonstrated that local stimulation could be manipulated to reprogram the deformation modes from leaning to the right to leaning to the left, and vice versa.

Fig. 6a shows a chiral SM-PDMS 3D hollow cylinder folded using a 2D chiral SM-PDMS with 12 × 4 unit cells with w and h of 4 and 20 mm, respectively. The 3D cylindrical chiral SM-PDMS exhibited imperfection-dependent deformation modes: twisting clockwise or counterclockwise under a compressive load depending on the local stimulation region. Fig. 6a shows a typical reprogrammable cycle: the 3D chiral SM-PDMS twisted counterclockwise under a compressive load if local stimulation was applied to the region with $\alpha = 82°$; it recovered its original shape after receiving global light stimulation; thereafter, the 3D chiral SM-PDMS twisted clockwise under a compressive load if a local stimulation was applied to the region with $\alpha = 98°$. Fig. A2a and b show the preparation of a specimen via 3D printing and templating and the application of local stimulation using a photomask. Fig. 6b shows the sequence of progressively deformed shapes of the 3D chiral SM-PDMS specimen under five different compressive strain levels and different local stimulation (see the animation in Video S2). The deformation patterns of the experimental results correlate with the simulated results. In addition, the imperfection-dependent deformation modes were validated by quantitatively evaluating the stress-strain curves and twist angles under different compression strains. For the same 3D SM-PDMS specimen under different local stimulation, the two stress-strain curves almost overlapped with each other and were independent of local stimulation, whereas the twist angles showed opposite changing tendencies (see Fig. 6c and d). These results further demonstrated that the 3D cylindrical chiral SM-PDMS had reprogrammable twist deformation modes using local stimulation without sacrificing its stiffness.

4.3. Buckling-induced metamaterial

Finally, we created a buckling-induced SM-PDMS with a distinct rotational direction after different local stimulation. The buckling-induced SM-PDMS was a 2 × 2 array of hollow squares. The pattern is designed to allow the direction-changeable rotation and stability when placed on an uneven surface. To apply local stimulation, each square was diagonally divided into four parts, and local stimulation was applied to the two spaced parts of the four parts. Examples of applying two different local stimulations are shown in Fig. 7a, which also shows the method of applying loads to induce an overall structural compression (see the animation in Video S3). Instead of the uniaxial compressive load used in the previous two structures, a pneumatic load was used to power the deformation of the buckling-induced SM-PDMS. The pillars of the buckling-induced SM-PDMS underwent buckling by applying a vacuum (evacuation) to the four chambers, resulting in its deformation into bent shapes. The bending direction was predetermined by either material imperfections introduced by local stimulation or geometric imperfections introduced via pre-deformation, which consequently causes the center area to rotate in one preferred direction. Regarding material imperfections, FEM analyses were conducted on the structure, where the blue or green areas were set as the local stimulation regions (Fig. 7a). The results show a preferred clockwise or counterclockwise rotation was caused if local stimulation was applied to the blue or green regions, respectively (see Fig. 7b). Before fabrication, two geometric parameters (i.e., the width of each square w and the radius of each pore r) could be changed to tune the rotation angle and the required pressure. Fig. 7c shows the dependence of the rotation angle on the normalized radius

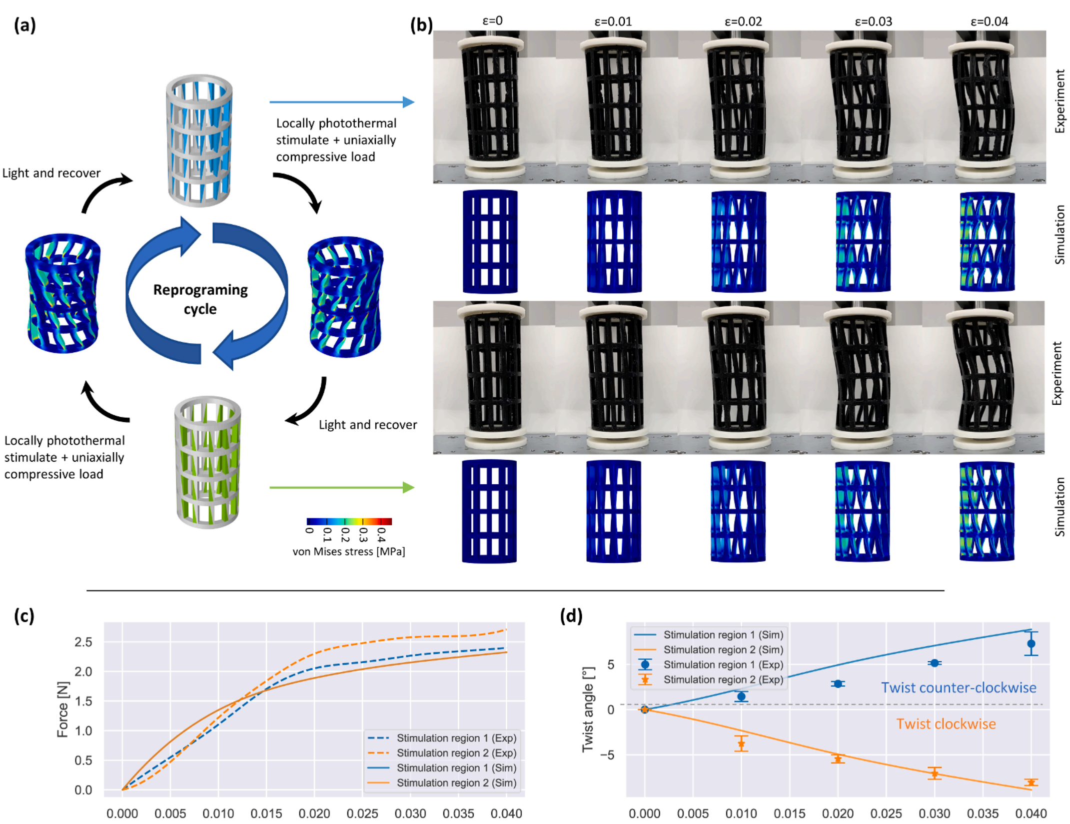

Fig. 6. 3D reprogrammable chiral metamaterial. (a) Typical reprogrammable cycle of a 3D chiral metamaterial that is capable of twisting either clockwise or counterclockwise based on different local stimulation. (b) Sequence of progressively deformed configurations of the 3D chiral metamaterial receiving different local stimulation. (c) Stress-strain curves of the 3D chiral metamaterial with different local stimulation under a compressive load. (d) Twist angle of the 3D chiral metamaterial with different local stimulation under a compressive load.

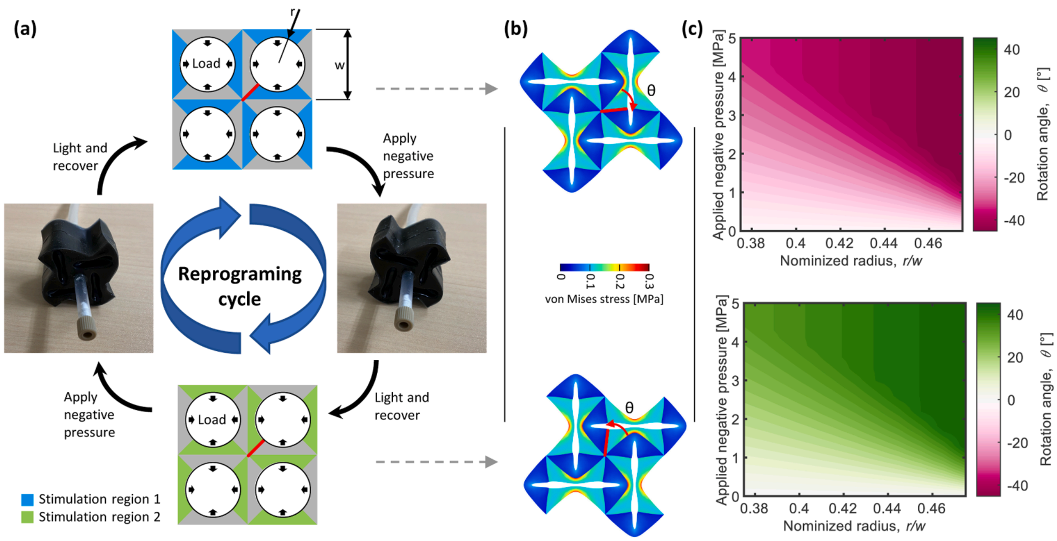

Fig. 7. Reprogrammable buckling-induced metamaterial. (a) Typical reprogrammable cycle of a 2D buckling-induced metamaterial that is capable of rotating either clockwise or counter-clockwise based on different local stimulation. The basic element is hollow squares whose rotation direction can be controlled using different local photothermal stimulation. (b) FEM results of the 2D buckling-induced metamaterial after different local stimulation. They show reversed rotation direction. (c) Tunable rotation angle of the 2D buckling-induced metamaterial based on different normalized radii and stimulation regions.

(r/w) and pressure, where w was set to 20 mm. These results showed that when the buckling-induced SM-PDMS was thoroughly deformed, the absolute value of the rotation angle reached a maximum of 45° when r/w approached 0.5, and gradually decreased to 30 ° as the r/w decreased to 0.38. In addition, the pressure required for deformation decreased as r/w increased.

We also fabricated a buckling-induced SM-PDMS prototype with w and r of 20 and 8.5 mm, respectively. Fig. A3a and b show the

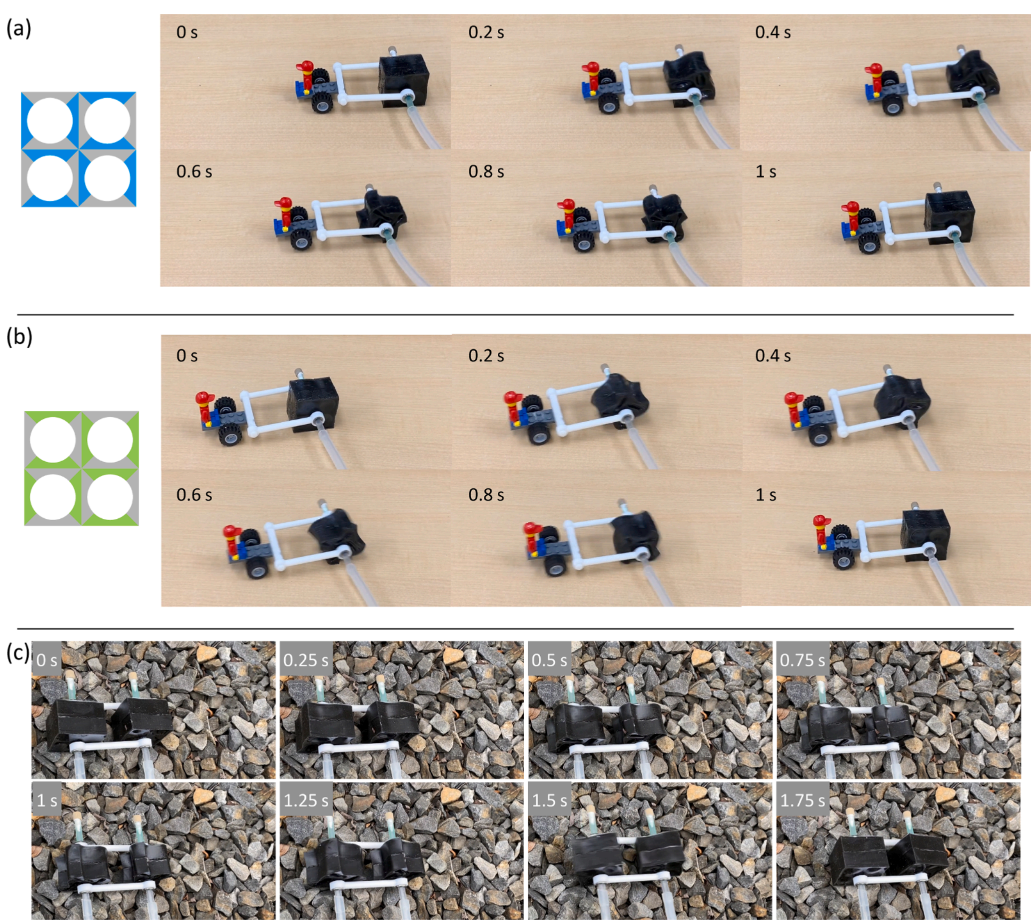

Fig. 8. Reprogrammable buckling-induced metamaterial actuator. (a and b) Using different local stimulation to change the moving direction (forward or backward) of an actuator made of buckling-induced metamaterial. (c) Assembling two actuators that are capable of moving on an uneven surface (a gravel road).

fabrication process and geometric size, respectively. Fig. A3c presents the method of applying local light stimulation on the prototype assisted with a photo mask. The buckling-induced SM-PDMS prototype was a pneumatic actuator that was powered using a simple syringe. After different local stimulation, the center of the actuator could rotate in one preferred direction when a vacuum was applied (see Fig. 7a). The center of the actuator rotated in reverse, and the actuator simultaneously recovered back to its original shape when the internal pressure was restored to ambient pressure. In addition, by taking advantage of the SM effect of the actuator, the preferred rotation could also be predetermined using geometric imperfections by applying a vacuum to a locally simulated actuator (i.e., applying a material imperfection) and then cooling to room temperature. The geometric imperfections could be cleared by applying light stimulation to the entire actuator. A typical reprogrammable cycle is shown in Fig. 7a.

A potential application of soft actuators is for the locomotion of soft robots. Figs. 8a and b show the demonstration of carrying cargo using the actuator with the preferred rotation direction out of geometric imperfection (see the animation in Video S3). The actuator, which was connected to a cargo, rotated 90° and moved during a single evacuation and pressurization cycle. During evacuation, the actuator shrunk, deformed into a gear-like shape, and simultaneously rotated 45°. The actuator continued to rotate 45° owing to inertia and gravity until a force balance was reached. During pressurization, the actuator gradually recovered to its original shape. Note that in contrast to most soft robots that could only move along one direction under the same drive, the actuator can move either forward or backward depending on the on-demand geometric imperfections, exhibiting more flexibility to tune the motion mode in soft robots. In addition, the actuators could be connected in series to form a soft robotic train that provides more transportation freedom. The soft robotic train was capable of locomotion on a relatively uneven surface because each actuator unit was self-propelled similar to a four-wheel-drive vehicle (Fig. 8c).

5. Conclusions

In summary, we showed that flexible metamaterials made of SM-PDMS can be reprogrammed into reversed deformation modes after fabrication. SM-PDMS, which is a rubber-like material with a SM effect, becomes softer after heating up to T_m and maintains a deformed shape after cooling. It can return to its original shape when heated again. Local simulation was achieved based on the photothermal effect by doping plasmonic titanium nitride nanoparticles into the SM-PDMS. Hence, the deformation modes of an SM-PDMS metamaterial can be encoded by the stiffness difference by programming the spatial distribution of the stimulation and non-stimulation regions. After cooling and maintaining the load, the preferred deformation mode remained. The deformation mode can be reprogrammed reversibly using distinctive local stimulation as the SM-PDMS metamaterial can return to its original shape when it receives global light stimulation. Specifically, we proposed three different SM-PDMS metamaterials with different mechanical responses: an auxetic SM-PDMS that can be reprogrammed from lateral contraction to lateral expansion under a uniaxial compressive load, a chiral SM-PDMS that can twist clockwise to counterclockwise under a uniaxial compressive load, and a buckling-induced SM-PDMS that can rotate clockwise to counterclockwise under a pneumatic load. In addition, we demonstrated an application using a buckling-induced SM-PDMS actuator. The soft actuator was capable of locomotion along a preferred direction after on-demand local stimulation. The actuator can be connected in series with a soft robotic train, and its distinctive deformation mode (shrinkage into a gear shape while rotating) makes it capable of moving on uneven surfaces.

The most significant feature of our designed mechanical metamaterials is their reprogrammability, which paves the way for their application in soft robots and other structural engineering fields. The changeable mechanical response rises additional deformation freedom and enhances their functionality. For example, the tubular auxetic SM-PDMS is a compliant structure that allows robots to overcome environmental challenges by deforming and conforming their bodies. Compared with the general auxetic compliant structures that only exhibit auxetic behavior, our designed tubular auxetic SM-PDMS exhibits both shrinkage (auxetic behavior) and expansion mechanical responses under compression, which thereby functions for exploration through unpredictable terrain [71]. Regarding the tubular chiral SM-PDMS, it can convert linear compressive motion into rotation, which is a rather unique feature of a machine. This unique actuation can be used for harnessing the interaction between materials and machines, and thus it is useful for placing them at the boundary acting as an actuator [72,73].

Furthermore, although we only focus on mechanical metamaterials with three different mechanical responses, our approach can be extended to arbitrary 2D and 3D structures to achieve more complicated deformation modes under different loads. Reprograming the deformation modes requires manually placing different photomasks for the sake of local light stimulation, which, however, brings about limitations in real applications where an automatic workflow is required. This limitation could be addressed by using other stimuli-responsive mechanical properties (e.g., magnetic response) which can also be accomplished by doping with other smart nanoparticles or using other smart polymeric materials [46,51,74].

Author contributions

X.Z. and K.U. contributed equally to this work. X.Z., K.U., and I.W. designed the research. X.Z., K.U., W-H.H., T-T.C., M.N., and I.W. performed the experiments. X.Z. performed the simulations. X.Z., K.U. and I.W prepared the manuscript. All authors analyzed the results and contributed to the manuscript.

Declaration of Competing Interest

The authors declare that they have no known competing financial interests or personal relationships that could have appeared to influence the work reported in this paper.

Acknowledgments

This work was supported by JST SPRING (Grant Number JPMJSP2124), Grant-in-Aid for JSPS Fellows DC2 (Grant Number 22J11202), the Innovative Science and Technology Initiative for Security (Grant Number JPJ004596, ATLA, Japan), and JST CREST (Grant Number JPMJCR19J3). The authors would like to thank Prof. Satoshi Ishii for providing the TiN nanoparticles and Dr. Siqian Wang for support in experiment.

Appendix A. Buckling analysis of a hybrid beam

A nonlinear buckling analysis was proposed to determine a suitable beam slenderness ratio (height to width ratio, h/w). The entire beam can be considered as a soft-rigid hybrid beam consisting of two bonded beams because half of the beam becomes softer after local stimulation. The theory of a beam on an elastic foundation can be used to study the buckling behavior of a hybrid beam, where the softer beam acts as the elastic foundation of the other beam [75–77]. For a simply supported hybrid beam subjected to a uniaxial compressive load, the critical compressive force N_{cr} can be expressed as [75]:

$$\frac{N_{cr}}{Dk^2} \approx \left(\frac{n\pi}{h_e k}\right)^2 + \left(\frac{n\pi}{h_e k}\right)^{-2} \tag{A.1}$$

where $D = E_r w_r^3/12(1-\upsilon_r^2)$ is the flexural rigidity of the rigid beam with Young's modulus E_r, width w_r, and Poisson's ratio υ_r. $k^{-1} = (2Dw_s(1+\upsilon_s)/3E_s)^{1/4}$ is the characteristic delay distance of the rigid beam on a soft Winkler foundation beam, with its spring stiffness determined by the width w_s, Poisson's ratio υ_s, and Young's modulus E_s of the soft beam. h_e is the equivalent height of the hybrid beam and is the beam height (h) for a simply supported beam. n is a positive integer that determines the buckling shape of a hybrid beam.

In this study, each beam can be assumed to be a fixed-fixed beam suffering from a uniaxial compressive load as the hybrid beams are assembled into a metamaterial. The equivalent height of a fixed-fixed beam was half its height ($h_e = h/2$). Assuming $w_r = w_s, E_r = 500E_s$, and $\upsilon_r = \upsilon_s$ for incompressibility, Eq. (A.1) can be solved using its slenderness ratio (h/w) as follows:

$$\frac{N_{cr}}{Dk^2} \approx \left(\left(\frac{500}{9}\right)^{1/4}\frac{n\pi}{h/w}\right)^2 + \left(\left(\frac{500}{9}\right)^{1/4}\frac{n\pi}{h/w}\right)^{-2}. \tag{A.2}$$

Clearly, the critical buckling force N_{cr} for a hybrid structure is not always minimized at the first order buckling shape with $n = 1$. Fig. A9 shows plots of the dimensionless buckling force as a function of h/w. Note that the critical buckling force fluctuates with h/w, and the beam tends to buckle in a high-order shape when $\frac{h}{w} > 12$. The slenderness ratio was set to 8, which corresponds to first order buckling (half-wave of a sinusoidal curve), to ensure that the beam deformed in the bending direction. In addition, the hybrid beam tended to bend in the direction of the rigid beam.

Supplementary material

Supplementary material associated with this article can be found, in the online version, at 10.1016/j.apmt.2022.101662

References

[1] K. Bertoldi, V. Vitelli, J. Christensen, M. Van Hecke, Flexible mechanical metamaterials, Nat. Rev. Mater. 2 (11) (2017) 1–11.
[2] X. Yu, J. Zhou, H. Liang, Z. Jiang, L. Wu, Mechanical metamaterials associated with stiffness, rigidity and compressibility: a brief review, Prog. Mater. Sci. 94 (2018) 114–173.
[3] M. Askari, D.A. Hutchins, P.J. Thomas, L. Astolfi, R.L. Watson, M. Abdi, M. Ricci, S. Laureti, L. Nie, S. Freear, et al., Additive manufacturing of metamaterials: a review, Addit. Manuf. 36 (2020) 101562.
[4] T.A. Schaedler, A.J. Jacobsen, A. Torrents, A.E. Sorensen, J. Lian, J.R. Greer, L. Valdevit, W.B. Carter, Ultralight metallic microlattices, Science 334 (6058) (2011) 962–965.
[5] X. Zheng, W. Smith, J. Jackson, B. Moran, H. Cui, D. Chen, J. Ye, N. Fang, N. Rodriguez, T. Weisgraber, et al., Multiscale metallic metamaterials, Nat. Mater. 15 (10) (2016) 1100–1106.
[6] X. Zheng, H. Lee, T.H. Weisgraber, M. Shusteff, J. DeOtte, E.B. Duoss, J.D. Kuntz, M.M. Biener, Q. Ge, J.A. Jackson, et al., Ultralight, ultrastiff mechanical metamaterials, Science 344 (6190) (2014) 1373–1377.
[7] M.C. Fernandes, J. Aizenberg, J.C. Weaver, K. Bertoldi, Mechanically robust lattices inspired by deep-sea glass sponges, Nat. Mater. 20 (2) (2021) 237–241.
[8] G.N. Greaves, A.L. Greer, R.S. Lakes, T. Rouxel, Poisson'S ratio and modern materials, Nat. Mater. 10 (11) (2011) 823–837.
[9] Z. Han, K. Wei, Multi-material topology optimization and additive manufacturing for metamaterials incorporating double negative indexes of poisson's ratio and thermal expansion, Addit. Manuf. (2022) 102742.
[10] S. Babaee, J. Shim, J.C. Weaver, E.R. Chen, N. Patel, K. Bertoldi, 3D Soft metamaterials with negative poisson's ratio, Adv. Mater. 25 (36) (2013) 5044–5049.
[11] X. Zheng, X. Guo, I. Watanabe, A mathematically defined 3D auxetic metamaterial with tunable mechanical and conduction properties, Mater. Des. 198 (2021) 109313.
[12] X. Zheng, T.-T. Chen, X. Guo, S. Samitsu, I. Watanabe, Controllable inverse design of auxetic metamaterials using deep learning, Mater. Des. 211 (2021) 110178.
[13] L. Zhou, X. Zheng, K. Du, X. Guo, Q. Yin, A. Lu, Y. Yi, Parametric and experiment studies of 3D auxetic lattices based on hollow shell cuboctahedron, Smart Mater. Struct. 30 (2) (2021) 025042.
[14] T. Frenzel, M. Kadic, M. Wegener, Three-dimensional mechanical metamaterials with a twist, Science 358 (6366) (2017) 1072–1074.
[15] Y. Zhang, B. Li, Q. Zheng, G.M. Genin, C. Chen, Programmable and robust static topological solitons in mechanical metamaterials, Nat. Commun. 10 (1) (2019) 1–8.
[16] C. Coulais, D. Sounas, A. Alu, Static non-reciprocity in mechanical metamaterials, Nature 542 (7642) (2017) 461–464.
[17] G. Librandi, E. Tubaldi, K. Bertoldi, Programming nonreciprocity and reversibility in multistable mechanical metamaterials, Nat. Commun. 12 (1) (2021) 1–9.
[18] C. Coulais, E. Teomy, K. De Reus, Y. Shokef, M. Van Hecke, Combinatorial design of textured mechanical metamaterials, Nature 535 (7613) (2016) 529–532.
[19] J.T. Overvelde, J.C. Weaver, C. Hoberman, K. Bertoldi, Rational design of reconfigurable prismatic architected materials, Nature 541 (7637) (2017) 347–352.
[20] Y. Liu, B. Shaw, M.D. Dickey, J. Genzer, Sequential self-folding of polymer sheets, Sci. Adv. 3 (3) (2017) e1602417.
[21] W. Liu, H. Jiang, Y. Chen, 3D Programmable metamaterials based on reconfigurable mechanism modules, Adv. Funct. Mater. 32 (9) (2022) 2109865.
[22] A. Rafsanjani, K. Bertoldi, A.R. Studart, Programming soft robots with flexible mechanical metamaterials, Sci. Rob. 4 (29) (2019) eaav7874.
[23] N. El-Atab, R.B. Mishra, F. Al-Modaf, L. Joharji, A.A. Alsharif, H. Alamoudi, M. Diaz, N. Qaiser, M.M. Hussain, Soft actuators for soft robotic applications: a review, Adv. Intell. Syst. 2 (10) (2020) 2000128.
[24] F. Schmitt, O. Piccin, L. Barbé, B. Bayle, Soft robots manufacturing: a review, Front. Robotic. AI 5 (2018) 84.
[25] D. Yang, B. Mosadegh, A. Ainla, B. Lee, F. Khashai, Z. Suo, K. Bertoldi, G. M. Whitesides, Buckling of elastomeric beams enables actuation of soft machines, Adv. Mater. 27 (41) (2015) 6323–6327.
[26] D. Goswami, S. Liu, A. Pal, L.G. Silva, R.V. Martinez, 3D-Architected soft machines with topologically encoded motion, Adv. Funct. Mater. 29 (24) (2019) 1808713.
[27] A. Pal, V. Restrepo, D. Goswami, R.V. Martinez, Exploiting mechanical instabilities in soft robotics: control, sensing, and actuation, Adv. Mater. 33 (19) (2021) 2006939.
[28] T. Chen, O.R. Bilal, K. Shea, C. Daraio, Harnessing bistability for directional propulsion of soft, untethered robots, Proc. Natl. Acad. Sci. 115 (22) (2018) 5698–5702.
[29] R.F. Shepherd, F. Ilievski, W. Choi, S.A. Morin, A.A. Stokes, A.D. Mazzeo, X. Chen, M. Wang, G.M. Whitesides, Multigait soft robot, Proc. Natl. Acad. Sci. 108 (51) (2011) 20400–20403.
[30] Q. Liu, W. Wang, M.F. Reynolds, M.C. Cao, M.Z. Miskin, T.A. Arias, D.A. Muller, P. L. McEuen, I. Cohen, Micrometer-sized electrically programmable shape-memory actuators for low-power microrobotics, Sci. Rob. 6 (52) (2021) eabe6663.
[31] B. Jin, H. Song, R. Jiang, J. Song, Q. Zhao, T. Xie, Programming a crystalline shape memory polymer network with thermo-and photo-reversible bonds toward a single-component soft robot, Sci. Adv. 4 (1) (2018) eaao3865.
[32] M.A. Skylar-Scott, J. Mueller, C.W. Visser, J.A. Lewis, Voxelated soft matter via multimaterial multinozzle 3D printing, Nature 575 (7782) (2019) 330–335.
[33] S. Waitukaitis, R. Menaut, B.G.-g. Chen, M. Van Hecke, Origami multistability: from single vertices to metasheets, Phys. Rev. Lett. 114 (5) (2015) 055503.
[34] T.J. Cui, M.Q. Qi, X. Wan, J. Zhao, Q. Cheng, Coding metamaterials, digital metamaterials and programmable metamaterials, Light Sci. Appl. 3 (10) (2014). e218–e218
[35] H.-F. Zhang, H. Zhang, Y. Yao, J. Yang, J.-X. Liu, A band enhanced plasma metamaterial absorber based on triangular ring-shaped resonators, IEEE Photonic. J. 10 (4) (2018) 1–10.
[36] H. Zhang, J. Yang, H. Zhang, J. Liu, Design of an ultra-broadband absorber based on plasma metamaterial and lumped resistors, Opt. Mater. Express 8 (8) (2018) 2103–2113.
[37] X. Fang, J. Wen, L. Cheng, D. Yu, H. Zhang, P. Gumbsch, Programmable gear-based mechanical metamaterials, Nat. Mater. 21 (2022) 869–876.
[38] B. Florijn, C. Coulais, M. van Hecke, Programmable mechanical metamaterials, Phys. Rev. Lett. 113 (17) (2014) 175503.
[39] Y. Bai, C. Liu, Y. Li, J. Li, L. Qiao, J. Zhou, Y. Bai, Programmable mechanical metamaterials with tailorable negative poisson's ratio and arbitrary thermal

expansion in multiple thermal deformation modes, ACS Appl. Mater. Interfaces 14 (31) (2022) 35905–35916.
[40] Z. Meng, M. Liu, H. Yan, G.M. Genin, C.Q. Chen, Deployable mechanical metamaterials with multistep programmable transformation, Sci. Adv. 8 (23) (2022) eabn5460.
[41] B. Jenett, C. Cameron, F. Tourlomousis, A.P. Rubio, M. Ochalek, N. Gershenfeld, Discretely assembled mechanical metamaterials, Sci. Adv. 6 (47) (2020) eabc9943.
[42] A. Bossart, D.M. Dykstra, J. Van der Laan, C. Coulais, Oligomodal metamaterials with multifunctional mechanics, Proc. Natl. Acad. Sci. 118 (21) (2021).
[43] J. Mueller, J.A. Lewis, K. Bertoldi, Architected multimaterial lattices with thermally programmable mechanical response, Adv. Funct. Mater. 32 (1) (2022) 2105128.
[44] S. Janbaz, K. Narooei, T. Van Manen, A. Zadpoor, Strain rate–dependent mechanical metamaterials, Sci. Adv. 6 (25) (2020) eaba0616.
[45] H. Lee, Y. Jang, J.K. Choe, S. Lee, H. Song, J.P. Lee, N. Lone, J. Kim, 3D-Printed programmable tensegrity for soft robotics, Sci. Robot. 5 (45) (2020) eaay9024.
[46] Y. Kim, H. Yuk, R. Zhao, S.A. Chester, X. Zhao, Printing ferromagnetic domains for untethered fast-transforming soft materials, Nature 558 (7709) (2018) 274–279.
[47] F. Pan, Y. Li, Z. Li, J. Yang, B. Liu, Y. Chen, 3D Pixel mechanical metamaterials, Adv. Mater. 31 (25) (2019) 1900548.
[48] T. Chen, M. Pauly, P.M. Reis, A reprogrammable mechanical metamaterial with stable memory, Nature 589 (7842) (2021) 386–390.
[49] Y. Wang, L. Li, D. Hofmann, J.E. Andrade, C. Daraio, Structured fabrics with tunable mechanical properties, Nature 596 (7871) (2021) 238–243.
[50] J.A. Jackson, M.C. Messner, N.A. Dudukovic, W.L. Smith, L. Bekker, B. Moran, A. M. Golobic, A.J. Pascall, E.B. Duoss, K.J. Loh, et al., Field responsive mechanical metamaterials, Sci. Adv. 4 (12) (2018) eaau6419.
[51] S. Li, B. Deng, A. Grinthal, A. Schneider-Yamamura, J. Kang, R.S. Martens, C. T. Zhang, J. Li, S. Yu, K. Bertoldi, et al., Liquid-induced topological transformations of cellular microstructures, Nature 592 (7854) (2021) 386–391.
[52] S. Li, G. Librandi, Y. Yao, A.J. Richard, A. Schneider-Yamamura, J. Aizenberg, K. Bertoldi, Controlling liquid crystal orientations for programmable anisotropic transformations in cellular microstructures, Adv. Mater. 33 (42) (2021) 2105024.
[53] C. Yang, M. Boorugu, A. Dopp, J. Ren, R. Martin, D. Han, W. Choi, H. Lee, 4D Printing reconfigurable, deployable and mechanically tunable metamaterials, Mater. Horiz. 6 (6) (2019) 1244–1250.
[54] B. Zhang, H. Li, J. Cheng, H. Ye, A.H. Sakhaei, C. Yuan, P. Rao, Y.-F. Zhang, Z. Chen, R. Wang, et al., Mechanically robust and UV-curable shape-memory polymers for digital light processing based 4D printing, Adv. Mater. 33 (27) (2021) 2101298.
[55] M. Ebara, K. Uto, N. Idota, J.M. Hoffman, T. Aoyagi, Shape-memory surface with dynamically tunable nano-geometry activated by body heat, Adv. Mater. 24 (2) (2012) 273–278.
[56] Standard Test Methods for Vulcanized Rubber and Thermoplastic Elastomers-Tension, Standard, ASTM International, West Conshohocken, Pennsylvania, US, 2021.
[57] Standard Test Method for Assignment of the Glass Transition Temperature By Dynamic Mechanical Analysis, Standard, ASTM International, West Conshohocken, Pennsylvania, US, 2018.
[58] P. Fan, W. Chen, B. Zhao, J. Hu, J. Gao, G. Fang, F. Peng, Formulation and numerical implementation of tensile shape memory process of shape memory polymers, Polymer 148 (2018) 370–381.
[59] Y.-C. Chen, D.C. Lagoudas, A constitutive theory for shape memory polymers. part i: large deformations, J. Mech. Phys. Solids 56 (5) (2008) 1752–1765.
[60] Y.-C. Chen, D.C. Lagoudas, A constitutive theory for shape memory polymers. part II: a linearized model for small deformations, J. Mech. Phys. Solids 56 (5) (2008) 1766–1778.
[61] O.H. Yeoh, Some forms of the strain energy function for rubber, Rubber Chem. Technol. 66 (5) (1993) 754–771.
[62] I. Watanabe, A. Yamanaka, Voxel coarsening approach on image-based finite element modeling of representative volume element, Int. J. Mech. Sci. 150 (2019) 314–321.
[63] I. Watanabe, D. Setoyama, N. Nagasako, N. Iwata, K. Nakanishi, Multiscale prediction of mechanical behavior of ferrite–pearlite steel with numerical material testing, Int. J. Numer. Methods Eng. 89 (7) (2012) 829–845.
[64] H. Chu, C. Gu, S. Li, Y. Zhang, J. Bian, C. Jiang, Measuring the absorption of TiN metallic films using cathodoluminescence of GaN films, Opt. Mater. Express 7 (4) (2017) 1302–1309.
[65] A. Ishimaru, Wave propagation and scattering in random media, 2 academic press, New York (1978).
[66] M.F. Modest, S. Mazumder, Radiative heat transfer, Academic press, 2021.
[67] S. Ishii, K. Uto, E. Niiyama, M. Ebara, T. Nagao, Hybridizing poly (ε-caprolactone) and plasmonic titanium nitride nanoparticles for broadband photoresponsive shape memory films, ACS Appl. Mater. Interfaces 8 (8) (2016) 5634–5640.
[68] X. Ren, J. Shen, A. Ghaedizadeh, H. Tian, Y.M. Xie, A simple auxetic tubular structure with tuneable mechanical properties, Smart Mater. Struct. 25 (6) (2016) 065012.
[69] W. Wu, W. Hu, G. Qian, H. Liao, X. Xu, F. Berto, Mechanical design and multifunctional applications of chiral mechanical metamaterials: a review, Mater. Des. 180 (2019) 107950.
[70] T. Frenzel, J. Köpfler, E. Jung, M. Kadic, M. Wegener, Ultrasound experiments on acoustical activity in chiral mechanical metamaterials, Nat. Commun. 10 (1) (2019) 1–6.
[71] M.F. Simons, K.M. Digumarti, A.T. Conn, J. Rossiter, Tiled auxetic cylinders for soft robots. 2019 2nd IEEE International Conference on Soft Robotics (RoboSoft), IEEE, 2019, pp. 62–67.
[72] R.M. Erb, J.S. Sander, R. Grisch, A.R. Studart, Self-shaping composites with programmable bioinspired microstructures, Nat. Commun. 4 (1) (2013) 1–8.
[73] C. Coulais, As the extension, so the twist, Science 358 (6366) (2017) 994–995.
[74] A.H. Gelebart, D.J. Mulder, G. Vantomme, A.P. Schenning, D.J. Broer, A rewritable, reprogrammable, dual light-responsive polymer actuator, Angew. Chem. Int. Ed. 56 (43) (2017) 13436–13439.
[75] M. Hetényi, M.I. Hetbenyi, Beams on elastic foundation: Theory with applications in the fields of civil and mechanical engineering volume 16, University of Michigan press Ann Arbor, MI, 1946.
[76] B. Mukherjee, D.A. Dillard, On buckling of a thin plate on an elastomeric foundation, Int. J. Mech. Sci. 149 (2018) 429–435.
[77] L. Zhang, G. Wu, J. Wu, A kerr-type elastic foundation model for the buckling analysis of a beam bonded on an elastic layer, ZAMM-J. Appl. Math. Mech. Z. für Angew. Math. und Mech.. 99 (10) (2019) e201900162.
[78] A. Bezazi, F. Scarpa, C. Remillat, A novel centresymmetric honeycomb composite structure, Compos. Struct. 71 (3–4) (2005) 356–364.
[79] F.-Y. Huang, B.-H. Yan, D.-U. Yang, The effects of material constants on the micropolar elastic honeycomb structure with negative poisson's ratio using the finite element method, Eng. Comput. (Swansea) 19 (2002) 742–763.
[80] J.T.B. Overvelde, S. Shan, K. Bertoldi, Compaction through buckling in 2D periodic, soft and porous structures: effect of pore shape, Adv. Mater. 24 (17) (2012) 2337–2342.
[81] J. Shim, S. Shan, A. Košmrlj, S.H. Kang, E.R. Chen, J.C. Weaver, K. Bertoldi, Harnessing instabilities for design of soft reconfigurable auxetic/chiral materials, Soft Matter 9 (34) (2013) 8198–8202.
[82] A. Alderson, K.L. Alderson, D. Attard, K.E. Evans, R. Gatt, J.N. Grima, W. Miller, N. Ravirala, C. Smith, K. Zied, Elastic constants of 3-, 4-and 6-connected chiral and anti-chiral honeycombs subject to uniaxial in-plane loading, Compos. Sci. Technol. 70 (7) (2010) 1042–1048.
[83] A. Alderson, K. Alderson, G. Chirima, N. Ravirala, K. Zied, The in-plane linear elastic constants and out-of-plane bending of 3-coordinated ligament and cylinder-ligament honeycombs, Compos. Sci. Technol. 70 (7) (2010) 1034–1041.
[84] Y. Chen, F. Scarpa, Y. Liu, J. Leng, Elasticity of anti-tetrachiral anisotropic lattices, Int. J. Solids Struct. 50 (6) (2013) 996–1004.
[85] P. Ziemke, T. Frenzel, M. Wegener, P. Gumbsch, Tailoring the characteristic length scale of 3D chiral mechanical metamaterials, Extreme Mech. Lett. 32 (2019) 100553.